 CMES, vol.96, no.5, pp.293-316, 2013

The MLPG(5) for the Analysis of Transient Heat Transfer in the Frequency Domain

L. Godinho[1] **and D. Dias-da-Costa**[2]

Abstract: Transient heat conduction problems can be dealt with using different numerical approaches. In some recent papers, a strategy to tackle these problems using a frequency domain formulation has been presented and successfully applied associated to methods such as the BEM. Here a formulation of the meshless local Petrov-Galerkin (MLPG) is developed and presented to allow the analysis of such problems. The proposed formulation makes use of the RBF-based version of the MLPG and employs the Heaviside step function as the test function, leading to the so-called MLPG(5). In addition, the method is associated with a visibility criterion to allow the correct selection of neighbouring nodes for interpolation. This criterion greatly simplifies the incorporation of discontinuities, such as cracks or holes, into the numerical model, and allows handling more complex geometries. The model is verified and application examples are presented, illustrating the usefulness of the method in the analysis of realistic configurations.

Keywords: MLPG, Heaviside test function, Radial Basis Functions, Heat Transfer, Frequency domain.

1 Introduction

Transient heat conduction problems can arise in the design and analysis of different structures. Common examples include, for instance, the heat distribution and evolution during the construction of dams or other structures and the simulation of building heat losses and thermal bridges [see, for example, Branco *et al*. (2004)].

Typically, closed-form solutions are only known for extremely simple examples. Therefore, more complex numerical strategies are frequently required to deal with practical situations. The classical approaches tend to tackle this problem directly in the time domain [Chang *et al*. (1973); Shaw (1974); Wrobel and Brebbia (1981);

[1] CICC, Dept. Civil Engineering, University of Coimbra, Portugal.
[2] INESCC, University of Coimbra, and Dept. Civil Engineering, University of Coimbra, Portugal; School of Civil Engineering, The University of Sydney, NSW2006, Australia.

Dargush and Banerjee (1991)], whereas other approaches apply an inverse transformation to the solution derived in a transformed domain [Cheng *et al.* (1992); Zhu *et al.* (1994); Zhu and Satravaha (1996)], for instance using the Laplace transform. In this case, accuracy can be severely compromised by the inversion procedure if specific measures are not adopted. Both approaches have already been successfully applied using the finite element method (FEM), the finite difference method (FDM) and the boundary element method (BEM) over the years. More recently, meshless methods are gradually becoming very appealing due to the lack of mesh dependency and robustness in dealing with complex geometries [Liu and Gu (2001); Atluri (2004)]. Contributions can already be found, either in the time domain [Shibahara and Atluri (2011)], or in transformed domains [Wang *et al.* (2006)].

In order to avoid the limitations of the classical approaches, a different strategy was recently introduced using the Fourier transform. In this case, the transform can be applied directly to the governing differential equation and the solution is obtained for each frequency. The corresponding time-domain solution is then computed by means of the inverse Fourier transformation. The latter procedure was shown to avoid the accuracy drawbacks of the transformed domain approaches [António *et al.* (2005); Godinho *et al.* (2006)] and to be rather effective using the Boundary Element Method [Godinho *et al.* (2004;2006); Tadeu *et al.* (2006); Simões *et al.* (2012)] and the Method of Fundamental Solutions [Simões and Tadeu (2005); Godinho *et al.* (2006)]. However, since these approaches rely on the knowledge of fundamental solutions, the implementations are still constrained to simpler settings. For this reason, the authors herein propose an alternative comprehensive meshless framework which allows significantly extending the capabilities of the Fourier transformation procedure. For that purpose, the meshless local Petrov Galerkin (MLPG) method is adopted with Radial Basis Functions (RBFs) [Xiao and McCarthy (2003); Atluri (2004); Wendland (2009)]. It is highlighted that the choice of these interpolation functions is justified by the fact of being usually computationally cheaper than the MLS approach, and additionally satisfying the delta function property [Liu and Gu (2001); Shibahara and Atluri (2011)]. The latter property allows easily enforcing essential boundary conditions, thus avoiding penalty or Lagrange multiplier methods.

Many types of RBFs may be adopted, e.g. thin plate spline, Multiquadric (MQ) or Wendland type RBFs, some depending on a free (shape) parameter for which the adequate choice is not a closed topic [Fasshauer and Zhang (2007); Sarra and Sturghill (2009); Cheng (2012)]. Since this may influence the accuracy of the computed results, this is also addressed in the manuscript.

In the MLPG there is the possibility of conveniently selecting the test function,

leading to different classes of the method, usually identified by the abbreviation MLPG followed by a number [Atluri and Shen (2002)]. In this case, the Heaviside step function is adopted in order to circumvent the need to compute some of the required domain integrals in the weak-form of the Partial Differential Equation (PDE), leading to a MLPG(5) class method [Atluri and Shen (2002)]. Consequently, there is no need to define a mesh, either for interpolation or integration purposes. MLPG(5) methods have already been shown to be particularly accurate and robust in different problems [Atluri and Shen (2002); Atluri (2004)], being typically competitive with FEM or BEM approaches.

Finally, the implementation herein developed is also enhanced by a visibility criterion which allows selecting the relevant neighbouring nodes for interpolation, thus further extending the possibility of automatically dealing with complex geometries. The proposed approach is then thoroughly discussed and realistic application examples are presented, illustrating the usefulness and convergence capabilities of the method.

2 Mathematical formulation

2.1 Governing equations

To mathematically formulate the problem, we start by considering the standard time-dependent heat diffusion equation, which can be written as:

$$\nabla^2 T(\mathbf{x},t) = \frac{1}{K}\frac{\partial T(\mathbf{x},t)}{\partial t}, \tag{1}$$

where $T(\mathbf{x},t)$ is the temperature at domain point $\mathbf{x}$, $K = k/(\rho c)$ is the diffusivity, k, c and ρ are the thermal conductivity, specific heat and density, respectively.

Following previously published works [António *et al.* (2005); Godinho *et al.* (2004;2006); Simões and Tadeu (2005); Tadeu *et al.*(2011); Simões *et al.* (2012)] and considering an initial temperature distribution defined by $T_0(\mathbf{x})$, the application of a Fourier transformation to variable t allows writing equation (1) in the frequency domain as follows:

$$\nabla^2 \hat{T}(\mathbf{x},\omega) + \lambda^2 \hat{T}(\mathbf{x},\omega) = -\frac{T_0(\mathbf{x})}{K}, \text{ with } \lambda^2 = -\frac{\mathrm{i}\omega}{K}, \tag{2}$$

which is a frequency dependent equation, where $\omega = 2\pi f$ is the angular frequency; $\nabla^2 = \frac{\partial^2}{\partial x^2} + \frac{\partial^2}{\partial y^2}$ for 2D problems, and $\nabla^2 = \frac{\partial^2}{\partial x^2} + \frac{\partial^2}{\partial y^2} + \frac{\partial^2}{\partial z^2}$ for 3D problems. In this process, considering $T(\mathbf{x},t) = 0$ for $t<0$, the variable $\hat{T}(\mathbf{x},\omega) = \int_{-\infty}^{+\infty} T(\mathbf{x},t) e^{-\mathrm{i}\omega t} dt$ defines the Fourier transformed temperature.

In the latter equation, when $T_0(\mathbf{x}) = 0$ throughout the domain, the homogeneous Helmholtz equation is retrieved.

Different boundary conditions can be adopted, namely:

$$\hat{T}(\mathbf{x},\omega) = B(\mathbf{x},\omega) \quad \text{(Fourier transform of prescribed temperature)}, \tag{3}$$

$$\begin{aligned} \hat{q}_{\vec{n}}(\mathbf{x},\omega) &= -k\frac{\partial \hat{T}}{\partial \mathbf{n}}(\mathbf{x},\omega) \\ &= q(\mathbf{x},\omega) \quad \text{(Fourier transform of prescribed flux along } \mathbf{n}) \end{aligned} . \tag{4}$$

After solving equation (2) over a full range of frequencies, an inverse Fourier transformation may be applied to recover the response in the time domain. For this purpose, the following steps must be followed:

- the temperature variation curve at loaded boundaries must first be defined in the time domain;
- a FFT is then applied to this curve, obtaining its frequency domain transform;
- the response of the system at each point and at each frequency ($\hat{T}(\mathbf{x},\omega)$) must be scaled by the corresponding amplitude of the transformed curve;
- an inverse FFT is then applied to the scaled response, obtaining the time-domain temperature evolution curve at each point.

In this process, the Fast Fourier Transform (FFT) and inverse Fast Fourier Transform (iFFT) implementations provided in Matlab are used. Further details can also be found in Godinho *et al*. (2004) or António *et al*. (2005).

2.2 Formulation of the MLPG

The MLPG formulation herein adopted requires a set of points scattered throughout the domain and along its boundary. In this case, the following weak form of the governing equation around each node i is considered [Atluri (2004)]:

$$\int_{\Omega_i} \nabla^2 \hat{T}(\mathbf{x},\omega) v \, d\Omega + \int_{\Omega_i} \lambda^2 \hat{T}(\mathbf{x},\omega) v \, d\Omega = -\int_{\Omega_i} \frac{T_0(\mathbf{x})}{K} v \, d\Omega, \tag{5}$$

where Ω_i is the integration subdomain around the node i for the MLPG.

Considering that the test function v is the Heaviside step function (with unit value inside Ω_i and zero outside), and applying the divergence theorem to the first integral, the above equation can be rewritten in the more convenient form:

$$\begin{aligned} &\int_{\Gamma_{si}} \nabla\hat{T}(\mathbf{x},\omega).\mathbf{n}\, d\Gamma + \int_{\Gamma_{st}} \nabla\hat{T}(\mathbf{x},\omega).\mathbf{n}\, d\Gamma + \lambda^2 \int_{\Omega_i} \hat{T}(\mathbf{x},\omega) d\Omega = \\ &= -\int_{\Omega_i} \frac{T_0(\mathbf{x})}{K}\, d\Omega + \int_{\Gamma_{sf}} \frac{\bar{q}(\omega)}{k}\, d\Gamma \end{aligned} \quad , \tag{6}$$

in which Γ_s is the boundary of subdomain Ω_i around the node, which can be decomposed in Γ_{si} (internal boundary), Γ_{st} (essential conditions boundary) and Γ_{sf} (where $\bar{q}$ is imposed); $\hat{T}$ stands for the Fourier transform of the temperature and $\bar{q}$ is the imposed heat flow with respect to the normal direction ($\mathbf{n}$) to the boundary. A schematic representation of the local boundaries around differently located nodes is illustrated in Figure 1.

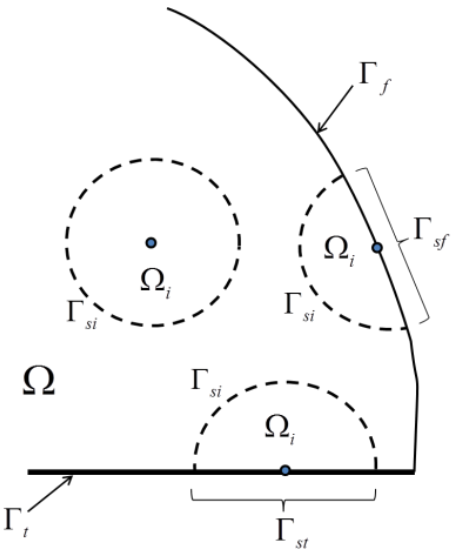

Figure 1: Illustrative representation of a portion of the MLPG domain of analysis, identifying the different local boundaries.

To approximate the solution of the PDE, a set of shape functions are built incorporating polynomial terms of the first order. Considering a point $\mathbf{x}$, and defining an interpolation domain around the point with M distinct nodes, the point temperature

can be defined by:

$$\hat{T}(\mathbf{x}) = \sum_{j=1}^{M} R^j(\mathbf{x}) \times B^j + \sum_{j=1}^{NP} P^j(\mathbf{x}) \times C^j, \tag{7}$$

with the following constraints:

$$\sum_{j=1}^{M} P^i(\mathbf{x}^j) \times B^j = 0, \text{for } i = 1..NP, \tag{8}$$

where R^j is the selected interpolation RBF, B^j and C^j are nodal amplitudes, NP equals 3 when the polynomial terms are of first order, in that case P^j being the j^{th} element of $\mathbf{P}(x,y) = [1\ x\ y]$.

The following different RBFs are tested in the present work:

$$R^j(\mathbf{x}) = r^2 \log(r) \quad \text{(thin plate spline RBF)}, \tag{9}$$

$$R^j(\mathbf{x}) = \sqrt{r^2 + c^2} \quad \text{(MQ RBF)}, \tag{10}$$

$$R^j(\mathbf{x}) = \left(1 - \frac{r}{r_0}\right)_+^4 \left(4\frac{r}{r_0} + 1\right) \quad \text{(Wendland's compact support RBF of order 2)}, \tag{11}$$

where 'c' is a shape parameter, r_0 is the radius of the support domain and $r = \left\|\mathbf{x} - \mathbf{x}^j\right\|$ in all cases.

Writing equations (7) and (8) for a set of M nodes ($\mathbf{x}^1$ to $\mathbf{x}^M$) within a local interpolation domain, the following system of equations can be defined:

$$\hat{\mathbf{T}} = \mathbf{R}_0 \mathbf{Q} \Leftrightarrow \mathbf{Q} = \mathbf{R}_0^{-1} \hat{\mathbf{T}} \tag{12}$$

where $\mathbf{R}_0$ is a matrix given by:

$$\mathbf{R}_0 = \begin{bmatrix} R^1(\mathbf{x}^1) & \cdots & R^M(\mathbf{x}^1) & P^1(\mathbf{x}^1) & \cdots & P^{NP}(\mathbf{x}^1) \\ \vdots & \ddots & \vdots & \vdots & \ddots & \vdots \\ R^1(\mathbf{x}^M) & \cdots & R^M(\mathbf{x}^M) & P^1(\mathbf{x}^M) & \cdots & P^{NP}(\mathbf{x}^M) \\ P^1(\mathbf{x}^1) & \cdots & P^1(\mathbf{x}^M) & 0 & 0 & 0 \\ \vdots & \ddots & \vdots & 0 & 0 & 0 \\ P^{NP}(\mathbf{x}^1) & \cdots & P^{NP}(\mathbf{x}^M) & 0 & 0 & 0 \end{bmatrix} \tag{13}$$

and $\hat{\mathbf{T}}$ is the vector containing the Fourier transformed temperatures at the nodal points of the interpolation domain and $\mathbf{Q} = [B^1 \ldots B^M\ C^1 \ldots C^{NP}]^T$.

The Fourier transformed temperature at a generic point $\mathbf{x}$, not necessarily coinciding with a node, can now be written as:

$$\hat{T}(\mathbf{x}) = \mathbf{R}^T(\mathbf{x})\mathbf{R}_0^{-1}\hat{\mathbf{T}} = \mathbf{\Phi}(\mathbf{x})\hat{\mathbf{T}}, \tag{14}$$

where $\mathbf{\Phi}(\mathbf{x}) = [\varphi^1(\mathbf{x}) \ \ ... \ \ \varphi^M(\mathbf{x})]$ are the nodal shape functions and $\mathbf{R} = [R^1(\mathbf{x}) \ ... \ R^M(\mathbf{x}) \ \ P^1(\mathbf{x}) \ ... \ P^{NP}(\mathbf{x})]^T$ is the vector containing the values of the RBFs and polynomial functions at point $\mathbf{x}$. It should be noted that the constructed shape functions in equation (14) possess the Kronecker's delta property.

The weak form in equation (6) replaces most of the necessary integrations (more importantly those involving second order derivatives) by boundary integrals at each subdomain, thus significantly reducing the computational effort and improving the accuracy. Using this weak form representation, the following system of equations can be defined:

$$(\mathbf{K} + \lambda^2\mathbf{C})\hat{\mathbf{T}}(\omega) = \hat{\mathbf{F}}(\omega), \tag{15}$$

where matrices $\mathbf{K}$ and $\mathbf{C}$ are independent of the frequency, $\hat{\mathbf{F}}$ stands for a vector containing the Fourier transform of both boundary conditions and external loads, and $\hat{\mathbf{T}}$ is the vector of unknown nodal temperatures in the frequency domain. The entries of these matrices and vectors can be defined as:

$$K_{ij} = \int_{\Gamma_{si}} \nabla\varphi^j(\mathbf{x}).\mathbf{n} \, d\Gamma + \int_{\Gamma_{st}} \nabla\varphi^j(\mathbf{x}).\mathbf{n} \, d\Gamma, \tag{16}$$

$$C_{ij} = \int_{\Omega_i} \varphi^j(\mathbf{x}) \, d\Omega, \tag{17}$$

$$F_i = -\int_{\Omega_i} \frac{T_0(\mathbf{x})}{K} \, d\Omega + \int_{\Gamma_{sf}} \frac{\bar{q}}{k} \, d\Gamma, \tag{18}$$

where $\varphi^j(\mathbf{x})$ stands for the shape function of node j.

If temperature $\bar{T}(\omega)$ is prescribed at a nodal point i, the corresponding entries in matrices $\mathbf{K}$ and $\mathbf{C}$, and in vector $\mathbf{F}$, can simply by written as:

$$K_{ij} = \delta_{ij}, \tag{19}$$

$$C_{ij} = 0, \tag{20}$$

$$F_i(\omega) = \bar{T}(\omega). \tag{21}$$

2.3 Support domain for interpolation

In the general case of a continuous domain, the choice of the neighbouring nodes for the interpolation is a trivial task, and usually those within a pre-defined distance (within the support domain) from the nodal point can be chosen. As suggested in several works (as in [Xiao and McCarthy (2003)]), this distance can be given by $d = a.r_{\min}$, where $r_{\min}$ is the distance from the nodal point to its closest neighbour and 'a' is an arbitrary parameter. In this case, the choice of very large values for 'a' can lead to densely populated equation systems, whilst small values may originate an insufficient number of points to construct the shape functions. Values between 2.5 and 5 are usually recommended [Xiao and McCarthy (2003); Atluri (2004)].

Although the above described process is quite straightforward to implement, and leads to accurate results in simple geometries, the presence of discontinuities in the domain (e.g. holes or cracks) can pose some problems in this interpolation. In fact, if a thin discontinuity is present, the above strategy can misleadingly select nodes which are on opposite sides of the discontinuity. To avoid this problem, the authors herein make use of the following algorithm for choosing the nodes for interpolation:

1. a "bounding box" is defined for the material domain under analysis, clearly identifying the physical boundaries including all discontinuities;
2. for each node, an initial approximation to the interpolation subdomain is obtained using the general procedure introduced above;
3. a line-of-sight analysis is performed between the analysis node and the nodes in the neighbouring interpolation subdomain;
4. only nodal points "visible" from the analysis node are included in the interpolation (e.g. those for which a line segment between the analysis node and the nodal point does not intersect any segment of the bounding box).

3 Accuracy of the model

3.1 Comparison with benchmark solutions

The accuracy and convergence of the proposed numerical model is first analysed by considering a simple problem consisting of a circular homogeneous domain with unit radius. The domain material has a density of 2500 kg/m^3, a conductivity of 1.4 W/m/^{o}K and a specific heat of 840 J/kg/^{o}K. Within this medium, at x=-0.75 m and y=0.0 m, a 2D point heat source is positioned (see Figure 3a). In the frequency

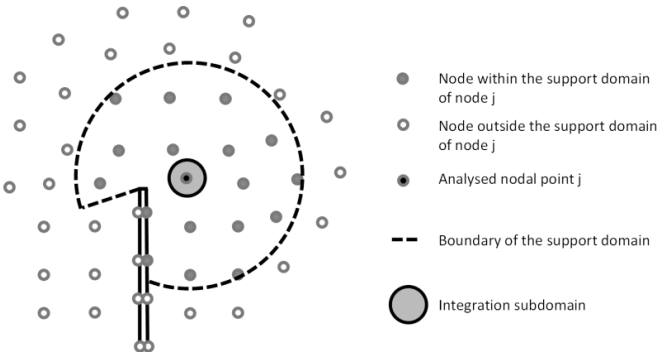

Figure 2: Sketch illustrating the support domain of a node in the presence of a material discontinuity.

domain, the effect of such source, positioned at $\mathbf{x}_s$, can be accounted assuming its contribution to be given by:

$$\hat{T}s(\mathbf{x},\mathbf{x}_s,\omega) = \frac{-\mathrm{i}}{4k} H_0^{(2)}\left(\lambda \left\|\mathbf{x}-\mathbf{x}_s\right\|\right), \tag{22}$$

where $H_0^{(2)}$ is the Hankel function of the second kind and order '0'.

The latter function corresponds to the fundamental solution of the homogeneous PDE obtained from equation (2) when $T_0(\mathbf{x}) = 0$. One should note that if the null frequency needs to be calculated, then the right-hand-side term in equation (15) cannot be computed. In this case, complex frequencies with a very small imaginary part must be used (see [António et al. (2005)] for details).

The proposed problem has been analysed making use of shape functions constructed using the three types of RBFs identified in equations (9)-(11). In the case of Wendland's RBF the support domain has the same radius as the interpolation domain at the node. In addition, different values of the free parameter are tested for the MQ RBF, trying to associate the optimal values to the average spacing between nodal points (h) by $c = L.h$ (see in Figures 3b-d the selected point distributions and corresponding average spacing). It should be noted that in the works of Xiao and McCarthy (2003), concerning 2D elasticity problems, a good value of this parameter was found to be obtained when $L = 6$. In all tests, the relative L2 error norm is used with the following definition:

$$e = \sqrt{\sum \left(\hat{T}_{exact} - \hat{T}_{numerical}\right)^2 / \sum \left(\hat{T}_{exact}\right)^2}. \tag{23}$$

Figure 4 exhibits the computed error (considering the nodal temperature values)

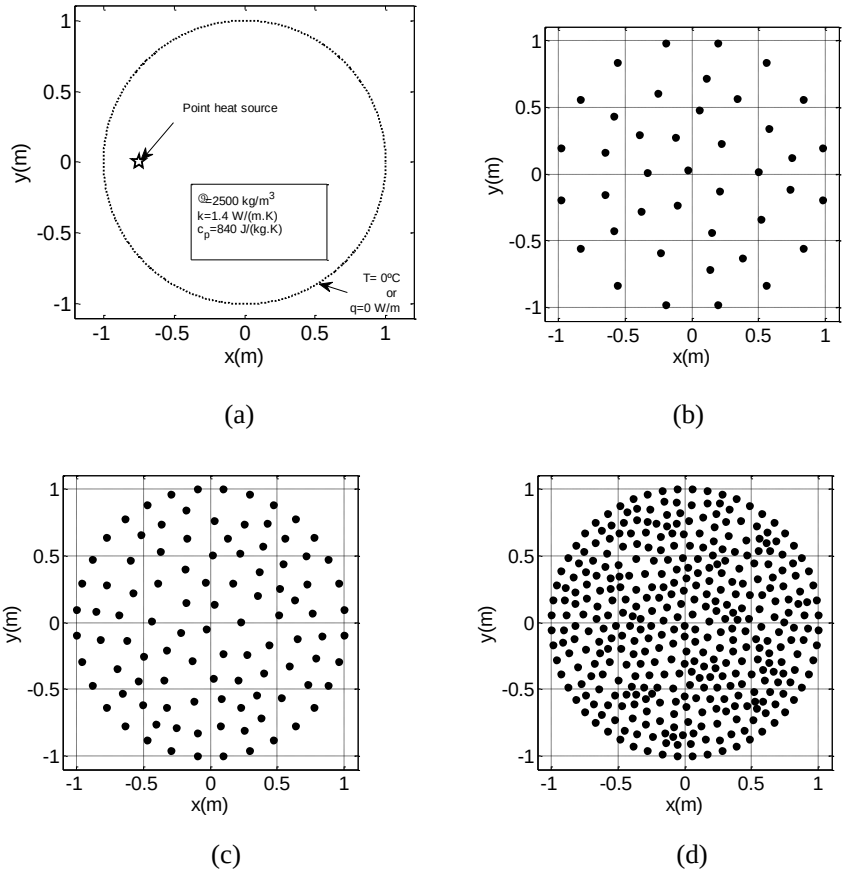

Figure 3: Model used for analysing the accuracy of the proposed approach, including: (a) a sketch of the problem geometry; and point distributions with: (b) h=0.4 m; (c) h=0.25 m; and (d) h=0.125 m.

for the MQ RBF and varying values of L, when the average spacing between nodal points is h=0.25 m (see Figure 3c). Two frequencies are analysed, namely $f = 1 \times 10^{-9}$ Hz and $f = 1 \times 10^{-5}$ Hz, together with two distinct boundary conditions, i.e., null temperatures (Figure 4a) and null fluxes (Figure 4b). The presented results reveal a clear trend for the response to improve with higher values of $L = c/h$. However, in Figure 4b, a minimum seems to occur for $L = 8$, after which the accuracy starts decreasing due to numerical instability. This value is somewhat higher than the one reported in [Xiao and McCarthy (2003)], indicating that for this type of problem it can be more adequate to consider slightly higher values than the

"optimal" ones observed in elasticity problems.

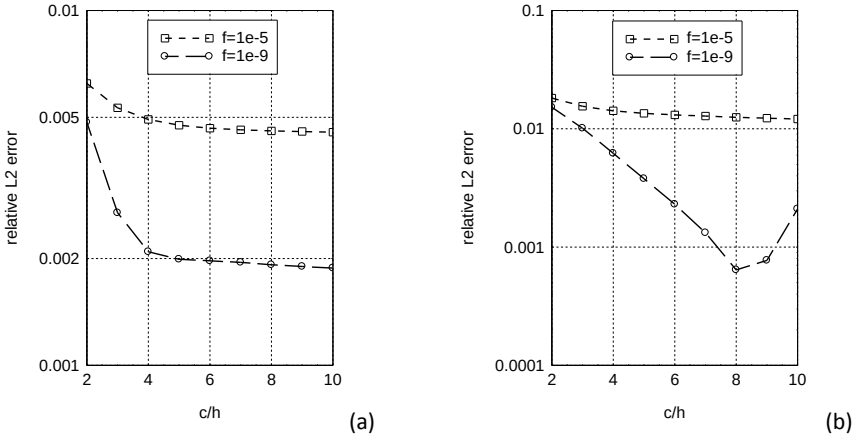

Figure 4: Relative L2 error as a function of the free parameter of the MQ RBF for a system with: (a) null boundary temperature; and (b) null flux boundary conditions.

Figure 5 illustrates the convergence of the response computed with the different RBFs. Again, two frequencies are analysed, namely $f = 1 \times 10^{-9}$ Hz and $f = 1 \times 10^{-5}$ Hz, both for null temperature and null flux boundary conditions.

The presented plots allow concluding that convergence is observed for the tested RBFs and for the MQ with two different shape parameter values. An exception occurs for the lower frequency when using the MQ RBF, for which case the convergence is not evident in the plotted results; however, even for that case, the computed results exhibit a very low error, which is less than 0.001 in the measured L2 error norm. Among the tested RBFs, it seems that Wendland's compact support RBF (here used with a support radius equal to the radius of the interpolation domain) provides the less accurate solutions, whereas the MQ RBF seems to provide the best overall accuracy in the calculation. Indeed, it can be seen that the MQ RBF has always the best performance in all tested cases, in particular when c=8h. The TPS RBF can be considered to be an intermediate performer, which is very close in terms of accuracy to the finite element solution (also presented in the plots). From all obtained results, it can be concluded that both the TPS and the MQ RBF are valid choices to build the MLPG shape functions, with better accuracy being given by the MQ. However, it must be stated that the presence of a shape parameter needing to be defined a-priori can pose some limitations to the use of these functions.

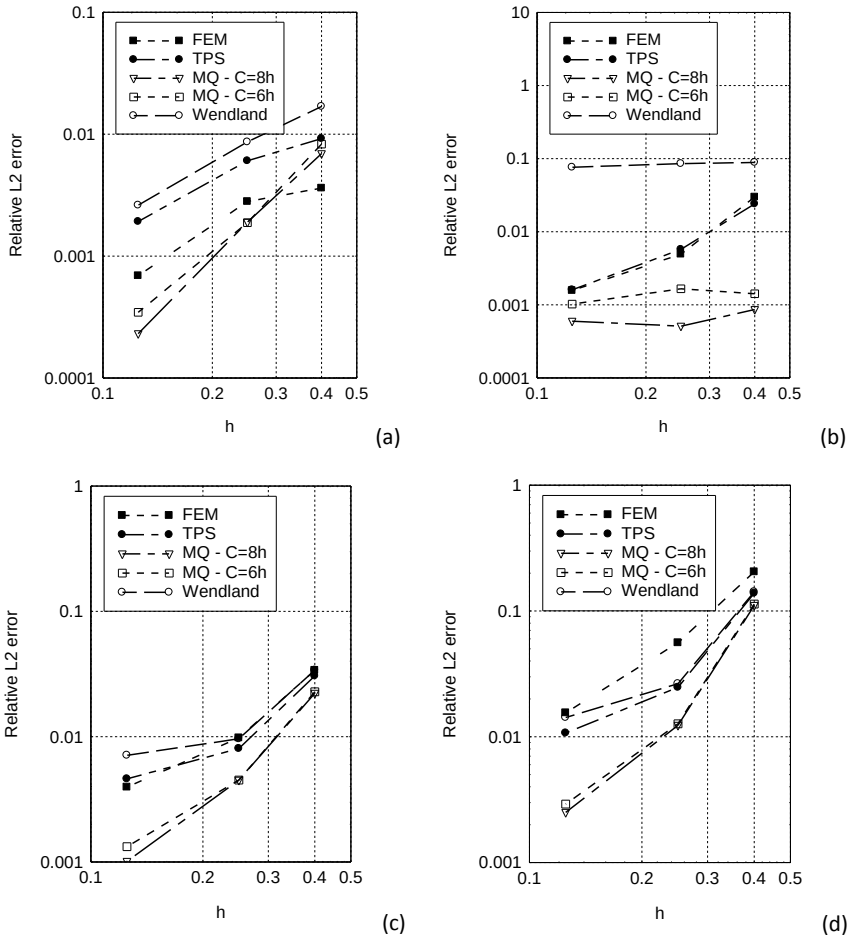

Figure 5: Relative L2 error for different choices of RBFs. On the left, a system with null boundary temperature is considered, whereas on the right null flux boundary conditions are assumed. (a) and (b) correspond to results for $f = 1 \times 10^{-9}$ Hz, whereas (c) and (d) correspond to $f = 1 \times 10^{-5}$ Hz.

3.2 Analysis of a non-trivial model

To further scrutinise the influence of the different RBFs and of a possible free parameter of those functions, a more complex configuration is now analysed. For this case, a rectangular domain with 2.0 m x 1.0 m, with a circular cavity of radius 0.5 m, is studied; as in the previous example, the solid domain has a density of 2500 kg/m^3, a conductivity of 1.4 W/m/^{o}K and a specific heat of 840 J/kg/^{o}K. Instead of

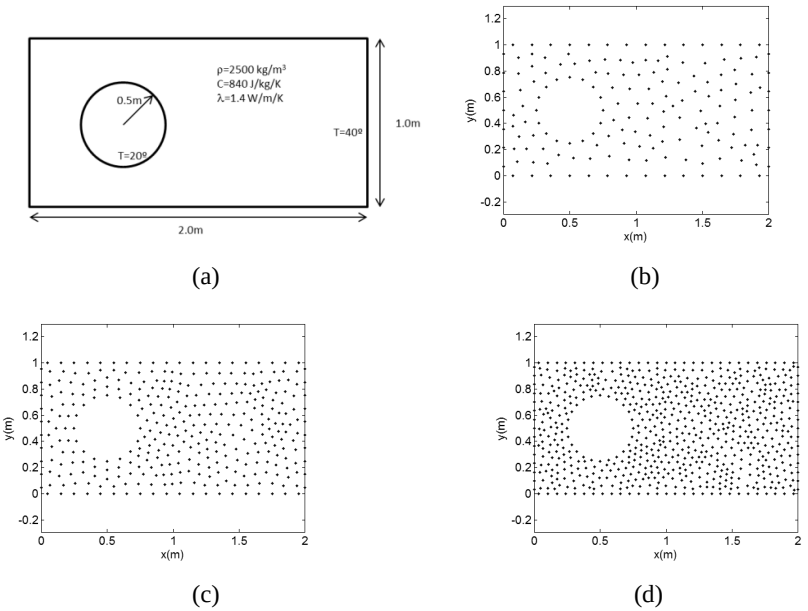

Figure 6: Non trivial domain used for assessing the accuracy of the MLP(5): (a) schematic representation; (b) point distribution PD1; (c) point distribution PD2; (d) point distribution PD3.

a domain source, boundary conditions corresponding to a fixed temperature of 40^o and of 20^o are enforced, respectively, at the right boundary and along the internal cavity's boundary; along the remaining boundaries, null fluxes are considered. This configuration is illustrated in Figure 6a.

Since no closed-form solution is known for this case, alternative strategies must be used to address the accuracy of the model. Here, a comparison is performed with a reference numerical solution computed with the Boundary Element Method [see, for example, Godinho et al. (2004)], using a discretisation with 400 elements. In the following analysis, frequencies ranging from $f = 1 \times 10^{-7}$ Hz to $f = 1 \times 10^{-5}$ Hz are analysed using three different point distributions, comprising, respectively, 166 (PD1), 342 (PD2) and 679 (PD3) points distributed throughout the domain and the boundary of the problem. These distributions are illustrated in Figures 6b, 6c and 6d.

Figure 7 illustrates the errors computed using the L2-norm defined in equation (20) with respect to the reference numerical solution. For this purpose, a full range of the RBF free parameter $c = L\,h$, with L ranging from 1 to 20 was considered. The

obtained results allowed selecting an optimal value of L, minimising the error norm at the full set of nodes. Clearly, the right column of Figure 7 reveals that the optimal value of the parameter depends on the analysed frequency. Moreover, in the case of a coarse point distribution (PD1), the variation can be significant, ranging from 14 at the lower frequency, to 5 at the higher frequencies. Nevertheless, for the less coarse distributions (PD2 and PD3) this variation is less noticeable, although still occurs. It is important to note from the obtained results, that no single "optimal" value of L can be defined covering all cases.

To assess the influence of this variation in the error norm, the left column on Figure 7 illustrates the error for the three distributions. Furthermore, for each distribution the following several curves are depicted using: a MQ with "optimal" L; a MQ with $L = 6$, as suggested by Xiao and McCarthy (2003); a MQ with $L = 8$, as adopted in the previous section; a TPS RBF; and a FEM model. In all plots, the solution computed using the TPS RBF is always less accurate than the ones computed with the MQ RBF, confirming the findings of the previous section; additionally, the FEM solution always presents lower accuracy than the MQ RBF, but it remains more accurate than the TPS RBF. Clearly, when using the MQ RBF in the MLPG(5) model, the results computed with $L = 8$ seem to be very close to those computed with the optimal L, and only for the PD3 (finer) distribution the difference between both cases becomes more evident. Again, this suggests that using $c = 8\,h$ as the free parameter of the MQ RBF is a very simple but quite good and safe strategy to tackle frequency domain heat transfer problems. However, if maximum accuracy is required, some strategies may be devised to optimise the value of the free parameter without requiring a reference solution. Recent works [Godinho and Tadeu (2012)] suggest a procedure based on the minimisation of the average domain residual to optimise this parameter; although in that case the authors apply that strategy to the so-called Kansa's method, this can be easily extended to the MLPG(5). It should be noted, however, that those alternatives require the problem to be solved for several values which are used to retrieve the "optimal" value or, alternatively, the use of elaborate and time-consuming optimisation routines.

4 Numerical applications

The proposed MLPG(5) formulation is herein applied to simulate transient heat conduction problems involving complex geometries. Two different configurations are addressed and discussed, considering for both cases a material with a density of 2500 kg/m^3, a conductivity of 1.4 W/m/K and a specific heat of 840 J/kg/K. It is highlighted that the MQ RBF is adopted in all cases. In addition, a total of 257 frequencies (including the null frequency) is used for the calculation, considering an increment of $\Delta f = 2.5 \times 10^{-6}$Hz, and using the heating curve described in Figure 8

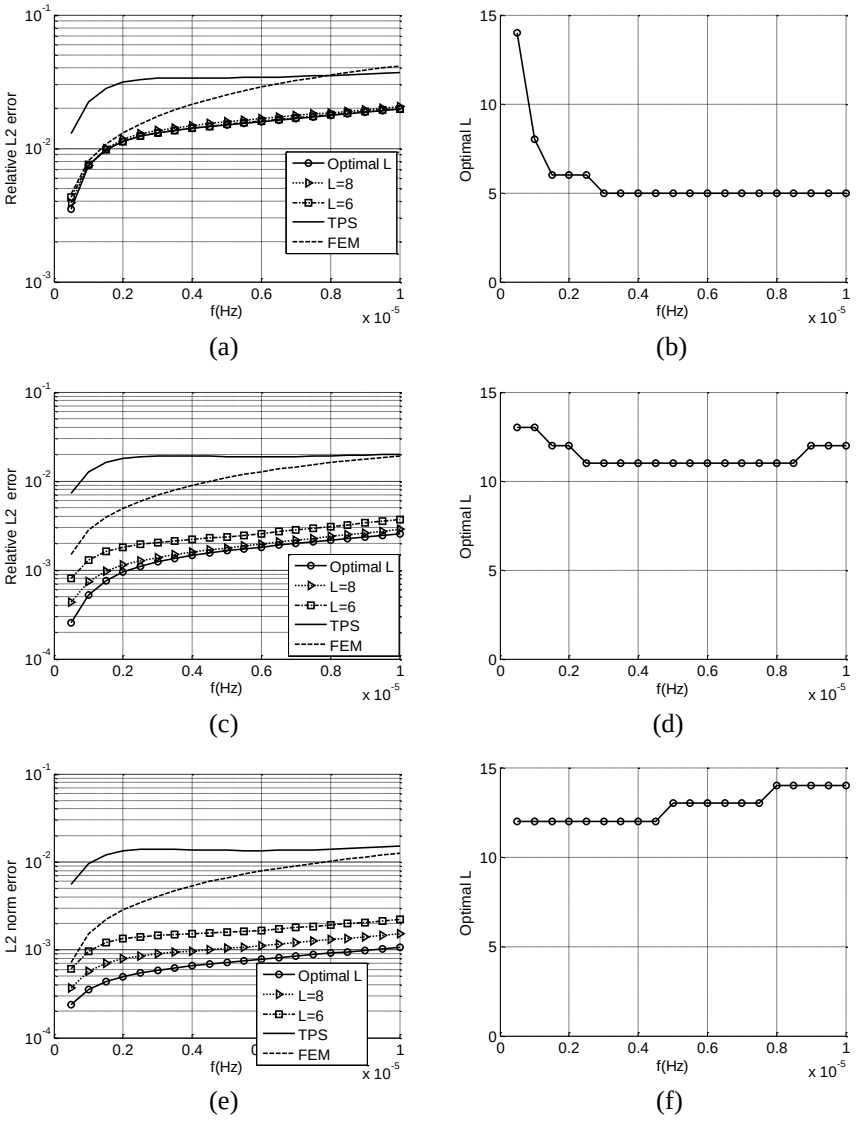

Figure 7: Results for the non-trivial test case using the PD1((a) and (b)), PD2((c) and (d)) and PD3((e) and (f)) point distributions. The left column exhibits the relative L2 error norm results and the right column exhibits the optimal values of L calculated for each frequency.

(in the time domain). A small numerical damping is introduced in the calculations, by using complex frequencies defined as $\omega_c = 2\pi f - 0.7 \times 2\pi\Delta f$, and its effect is later taken into account when computing the result in the time domain, by rescaling the time window by the factor $e^{0.7\times 2\pi\Delta f \times t}$.

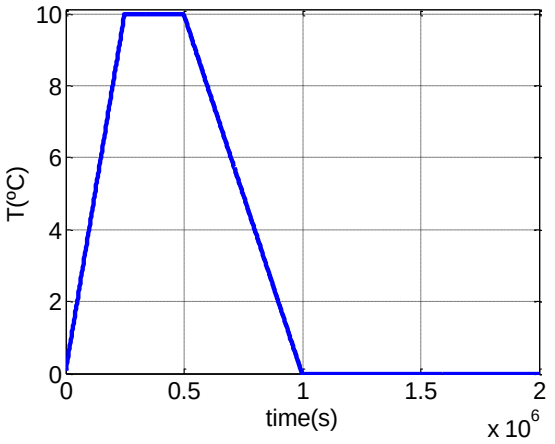

Figure 8: Heating curve used in the examples.

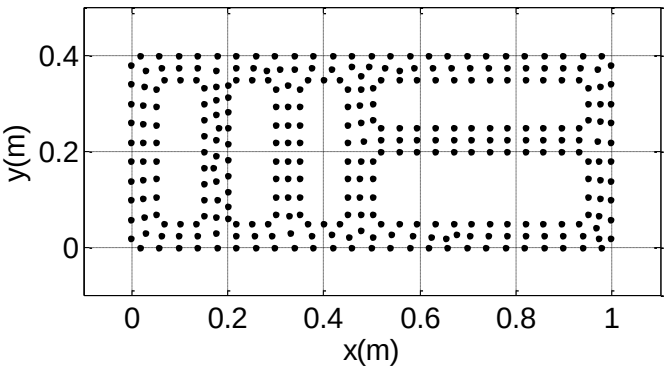

Figure 9: MLPG point distribution, using 311 points distributed throughout the domain and boundaries.

4.1 Rectangle with multiple cavities

The geometry selected for the first example consists of a rectangular block, with the properties defined above and incorporating a total of 5 holes. A total of 311

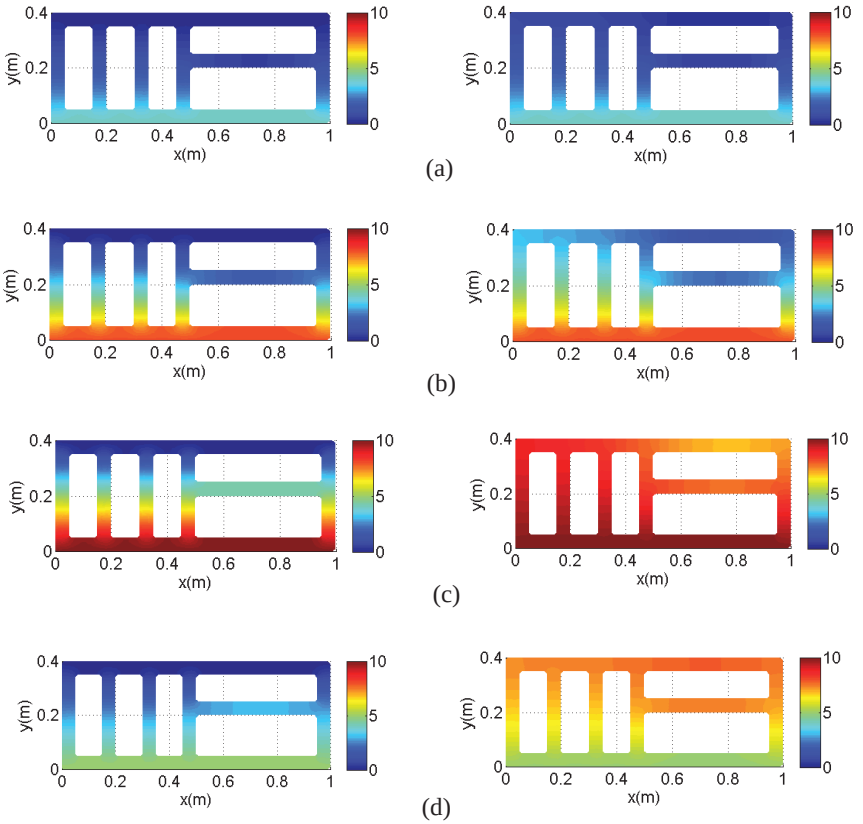

Figure 10: Temperature distribution for different time instants and for null temperatures (left) and flux (right) at the top boundary of the model: (a) $t = 0.1 \times 10^6$ s; (b) $t = 0.2 \times 10^6$ s; (c) $t = 0.5 \times 10^6$ s; and (d) $t = 0.75 \times 10^6$ s.

nodal points were scattered throughout the domain and boundaries, as shown in Figure 9. It should be noted that no special care was taken in order to enforce a regular distribution of those points. The heating curve represented in Figure 6 is imposed at the bottom of this model as a Dirichlet's boundary condition, whereas two different boundary conditions are tested at the top boundary of the model: null temperature or null heat flux.

Figure 10 illustrates the temperature distribution throughout the domain at different time instants, namely for $t = 0.1 \times 10^6$ s, $t = 0.2 \times 10^6$ s, $t = 0.5 \times 10^6$ s and $t = 0.75 \times 10^6$ s. At the first instant, the results for both top boundary conditions reveal very similar patterns, although a faster heating of the domain is already slightly noticeable in the case of null flux conditions (right column of Figure 10). As time

progresses, the differences between both cases become more visible, and the presence of non-zero temperatures at the top surface of the model for null flux conditions is evident in that case. For $t = 0.5 \times 10^6$ s, the model with null top temperature shows a progressive decrease of the temperature from bottom (10^oC) to top (0^oC), while much higher temperatures are visible for the null flux condition at the top region of the model. For the latter, it is interesting to note that the intermediate and top horizontal walls on the right side exhibit lower temperatures. This is due to the longer travel paths between the hot lower surface and those regions. For the last instant, already during the descending part of the heating curve, an inversion of the temperature profile between the two tested models is reported. In this case, the lower temperatures occur at the bottom, when null fluxes are enforced, and at the top, when null temperatures are enforced.

To validate the presented results, the same calculation was performed using a time marching semi-implicit algorithm (with $\Delta t = 250$ s) and a finite-element formulation (with a total of 2799 nodes). Comparison with the proposed model is presented in Figure 11a and 11b for a receiver located at x=0.7437 m and y=0.2184 m, also for the two tested cases. As can be seen, there is an excellent match between the two methods, with the temperature evolution computed in the time domain being almost identical for the two models. In Figures 11c and 11d the relative difference between the two models, calculated as $(T_{FEM} - T_{MLPG})/\max(T_{FEM})$, is illustrated. This confirms that the proposed method provides good results irrespectively of the presence of complex geometries, with maximum relative differences between methods of about 1.5% for the worst case.

4.2 Block with a thin crack

To further test the MLPG(5) model, a second example is considered which consists on a rectangular domain (1.0 m x 0.4 m) with a thin embedded crack. This model is described using 1170 nodal points and the visibility algorithm is applied in order to clearly identify the two sets of nodes placed on each side of the crack surface, thus avoiding interpolations between opposite sides. A global view of the model is shown in Figure 12a, and a detailed view of the crack region can be seen in Figure 12b. The heating curve of Figure 8 is applied at the leftmost surface of the model, whereas null flux is considered for all remaining surfaces (including crack surfaces).

Figure 13 shows the temperature distribution computed at two different time instants, one at $t = 0.3 \times 10^6$ s (at which the maximum temperature is reached at the left wall) and the other at $t = 0.6 \times 10^6$ s (when the temperature is decreasing at the left wall). The first stage ($t = 0.3 \times 10^6$ s) clearly shows that the maximum temperature has already been reached at the leftmost surface, whilst at the rightmost

surface lower temperatures are still registered. However, the most striking feature in this plot is the temperature disparity between both sides of the crack, clearly evidencing that no energy is crossing this surface and that a correct choice of interpolation points is being made. For the later time ($t = 0.6 \times 10^6$ s), slightly higher temperatures are registered at the right side of the model, whereas a visible temperature decrease is identified at the left boundary. The contrast between both sides of the crack is still noticed, while above the crack a perfect continuous temperature field can be observed.

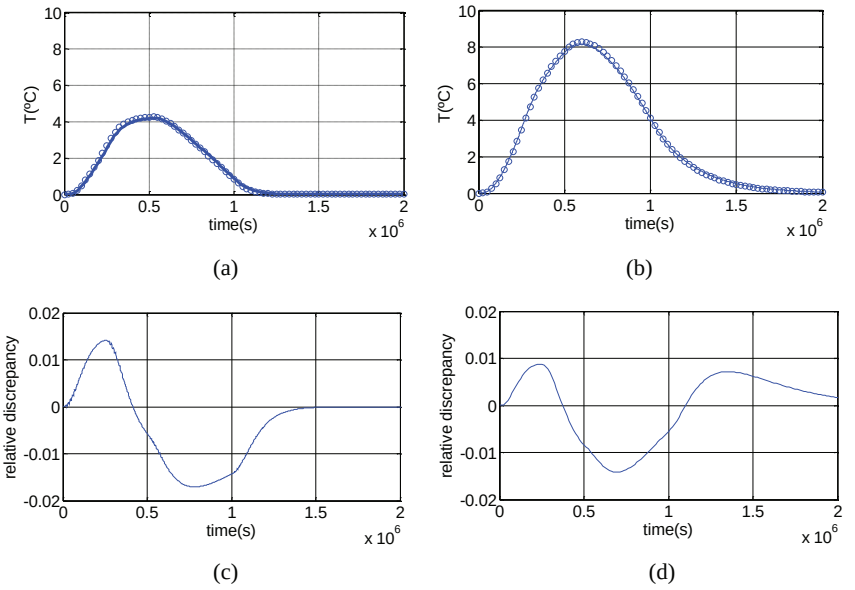

Figure 11: Comparison of the computed responses at a single receiver located at x=0.7437 m and y=0.2184 m for the case of null temperatures (a) and null fluxes (b) at the top boundary of the model (the continuous line represents the calculation using the proposed strategy, whereas the circular symbols are representing the response of a time marching FEM algorithm). In (c) and (d) the relative discrepancy between both responses is presented.

As in the previous case, the results have been computed at a specific domain point (now positioned at x=0.7796 m and y=0.3354 m) using a finite element time-marching algorithm. The corresponding results computed with that strategy and with the proposed method are illustrated in Figure 14a. As in the previous example, a perfect agreement is observed, with maximum relative discrepancies between the two approaches of less than 1% (Figure 14b).

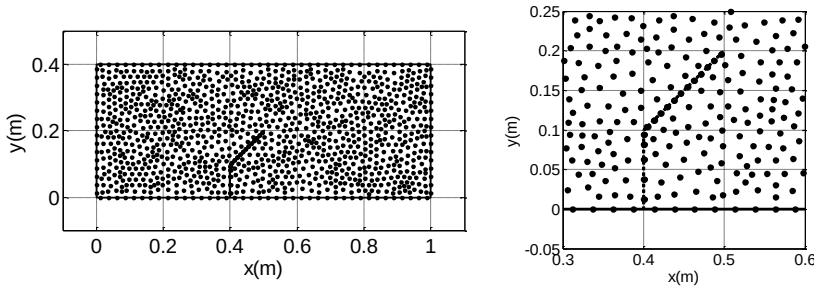

(a) (b)

Figure 12: Second example, consisting of a rectangular domain with a thin crack: (a) global geometry and point distribution; and (b) detail of the point distribution around the thin crack.

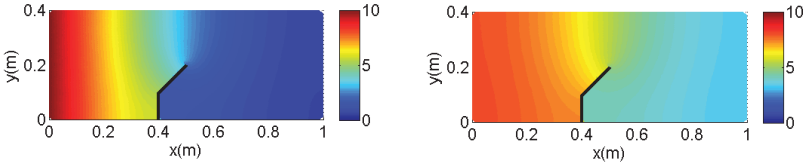

(a) (b)

Figure 13: Temperature distribution along the domain for: (a) $t = 0.3 \times 10^6$ s; and (b) $t = 0.6 \times 10^6$ s.

5 Final remarks

The use of the Fourier transform for solving transient heat transfer problems can be found in the literature. However, existing contributions are usually limited concerning the complexity of the tackled problems. This fact is naturally related with the limitations inherited from the adopted numerical framework (e.g. the boundary element method (BEM) or the method of fundamental solutions (MFS)). Aiming at solving these limitations, an entirely general framework was herein proposed, which promptly tackles complex geometric settings typically found in real problems and can handle imposition of initial conditions without requiring additional strategies. In addition, the proposed framework can be easily extended to incorporate space-dependent thermal properties, which are typically cumbersome to implement in BEM or MFS models. In this scope, it was proposed and discussed the implementation of the Meshless local Petrov-Galerkin for transient heat diffusion problems using the Heaviside test (MLPG(5)) function and RBFs to construct the

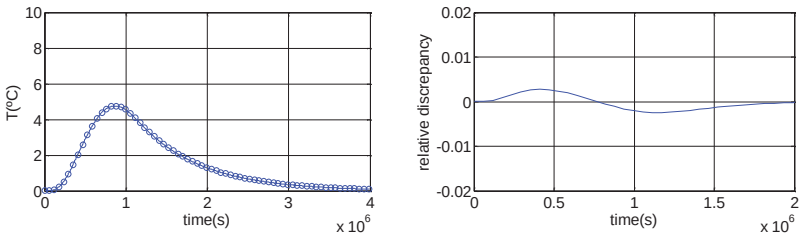

(a) (b)

Figure 14: In (a) the computed responses at a single receiver located at x=0.7796 m and y=0.3354 m are represented (the continuous line represents the calculation using the proposed strategy, whereas the circular symbols are representing the response of a time marching FEM algorithm). In (b), the relative discrepancy between both responses is presented.

shape functions. In this approach, the solution of the problem is calculated in a transformed (frequency) domain.

The proposed method was tested for different types of RBFs, and comparison with reference results obtained using a closed-form solution revealed that good responses can be retrieved. Among the tested RBFs, it was found that the MQ RBF can be a good choice, with accurate results and a fast convergence. Furthermore, it was also observed that, in this case, a good choice of the shape parameter can be $c = 8\,h$, which is somewhat higher than what is usually suggested for elasticity problems. The topic of the selection of this parameter is not a closed matter and may require the use of optimisation algorithms if high accuracy is needed. It should also be highlighted that results computed with the TPS RBF also evidenced a good accuracy, although with lower convergence rates.

The method was also applied to calculate the evolution of the temperature within complex shaped domains, incorporating multiple holes or a crack, for which a visibility algorithm was also implemented to avoid erroneous choices of the interpolating neighbours. Comparison with a standard time-marching algorithm applied together with finite element models also revealed the good accuracy of the method. One should note that, in this case, the response is first calculated in the frequency domain and then transformed to time domain by means of an inverse FFT.

Finally, it must be mentioned that the implemented method is truly meshless, since no connectivity between nodes is required, neither it becomes necessary to use any kind of background mesh for integration purposes.

Acknowledgement: The first author acknowledges the support provided by COMPETE and FCT (Fundação para a Ciência e Tecnologia, Portugal) under project PTDC/ECM/114189/2009. This work has also been framed under the Initiative Energy for Sustainability of the University of Coimbra and supported by the Energy and Mobility for Sustainable Regions - EMSURE - Project (CENTRO-07-0224-FEDER-002004).

References

António, J.; Tadeu, A.; Godinho, L.; Simões, N. (2005): Benchmark solutions for three-dimensional transient heat transfer in two-dimensional environments via the time Fourier transform. *Computers, Materials, Continua (CMC):* vol. 2, no. 1, pp.1-12.

Atluri, S. N. (2004): *The Meshless Local Petrov-Galerkin (MLPG) Method*. Tech. Science Press.

Atluri, S. N.; Shen, S. (2002): The Meshless Local Petrov-Galerkin (MLPG) Method: A Simple & Less-costly Alternative to the Finite Element and Boundary Element Methods. *CMES*, vol. 3, no. 1, pp. 11-51.

Branco, F. G.; Tadeu, A.; Simões, N. (2004): Heat conduction across double brick walls via BEM. *Building and Environment*, vol. 39, pp. 51-58.

Chang, Y. P.; Kang, C. S.; Chen, D. J. (1973): The use of fundamental Green functions for solution of problems of heat conduction in anisotropic media. *Int. J. Heat and Mass Transfer*, 16, pp. 1905-1918.

Cheng, A. H.-D. (2012): Multiquadric and its shape parameter - A numerical investigation of error estimate, condition number, and round-off error by arbitrary precision computation. *Eng. Anal. Bound. Elmts*., vol. 36, pp. 220-239.

Cheng, A. H.-D.; Abousleiman, Y.; Badmus, T. (1992): A Laplace transform BEM for axysymmetric diffusion utilizing pre-tabulated Green's function. *Eng. Anal. Bound. Elmts.*, vol. 9, pp. 39-46.

Dargush, G. F.; Banerjee, P. K. (1991): Application of the boundary element method to transient heat conduction. *Int. J. Numerical Methods in Engineering*, vol. 31, pp. 1231-1247.

Fasshauer, G. E.; Zhang, J. G. (2007): On choosing "optimal" shape parameters for RBF approximation. *Numerical Algorithms*, vol. 45, no. 1-4, pp. 345-368.

Godinho, L.; Tadeu, A.; Simões, N. (2004): Study of transient heat conduction in 2.5D domains using the Boundary Element Method. *Eng. Anal. Bound. Elmts.*, vol. 28, no. 6, pp. 593-606.

Godinho, L.; Tadeu, A.; Simões, N. (2006): "Accuracy of the MFS and BEM

on the analysis of acoustic wave propagation and heat conduction problems". In Sladek, J., & Sladek, V. (editors): *Advances in Meshless Methods*, Tech Science Press, Encino, California, pp. 177-198.

Godinho, L.; Tadeu, A. (2012): "Acoustic analysis of heterogeneous domains coupling the BEM with Kansa's method". *Eng. Anal. Bound. Elmts.*, 36, pp. 1014–1026.

Liu, G. R.; Gu, Y. T. (2001): A point interpolation method for two-dimensional solids. *International Journal for Numerical Methods in Engineering*, vol. 50, no. 4, pp. 937-951.

Sarra, S. A.; Sturgill, D. (2009): A random variable shape parameter strategy for radial basis function approximation methods. *Eng. Anal. Bound. Elmts*., vol. 33, pp. 1239-1245.

Shaw, R. P. (1974): An integral equation approach to diffusion. *Int. J. Heat and Mass Transfer*, vol. 17, pp. 693-699.

Shibahara, M.; Atluri, S. N. (2011): The meshless local Petrov-Galerkin method for the analysis of heat conduction due to a moving heat source, in welding. *International Journal of Thermal Sciences*, vol. 50, no. 6, pp. 984-992.

Simões, N.; Tadeu, A. (2005): Fundamental solutions for transient heat transfer by conduction and convection in an unbounded, half-space, slab and layered media in the frequency domain. *Eng. Anal. Bound. Elmts*., vol. 29, no. 12, pp. 1130-1142.

Simões, N.; Tadeu, A.; António, J.; Mansur, W. (2012): Transient heat conduction under nonzero initial conditions: a solution using the boundary element method in the frequency domain. *Eng. Anal. Bound. Elmts.,* vol. 36, no. 4, pp. 562-567.

Tadeu, A.; Simões, I.; Simões, N.; Prata, J. (2011): Simulation of dynamic linear thermal bridges using a boundary element method model in the frequency domain. *Energy and Buildings*, vol. 42, pp. 3685-3695.

Wang, H.; Qin, Q-H.; Kang, Y-L. (2006): A meshless model for transient heat conduction in functionally graded materials. *Computational Mechanics*, vol. 38, pp. 51-60.

Wendland, H. (2009): Meshless Galerkin methods using radial basis functions. *Mathematics of Computation*, vol. 68, no. 228, pp. 1521-1531.

Wrobel, L. C.; Brebbia, C. A. (1981): A formulation of the boundary element method for axisymmetric transient heat conduction. *Int. J. Heat and Mass Transfer*, vol. 24, pp.843-850..

Xiao, J. R.; McCarthy, M. A. (2003): A local Heaviside weighted meshless method for two-dimensional solids using radial basis functions. *Computational*

Mechanics, vol. 31, pp. 301–315.

Zhu, S. P., Satravaha, P., Lu, X. (1994): Solving the linear diffusion equations with the dual reciprocity methods in Laplace space. *Eng. Anal. Bound. Elmts.*, vol. 13, pp. 1-10.

Zhu, S. P.; Satravaha, P. (1996): An efficient computational method for nonlinear transient heat conduction problems. *Appl. Mathematical Modeling*, vol. 20, pp. 513-522.